CYBERNETICS AND PHYSICS, VOL. 14, NO. 3, 2025, 292–298

NONLINEAR CONTROL PROBLEMS OF SPACE ROBOT IN SERVICING GEOSTATIONARY SATELLITES

Yevgeny Somov
Navigation, Guidance and Control
Samara State Technical University
Samara, Russia
e_somov@mail.ru

Sergey Somov
Navigation, Guidance and Control
Samara State Technical University
Samara, Russia
s_somov@mail.ru

Sergey Butyrin
Navigation, Guidance and Control
Samara State Technical University
Samara, Russia
butyrinsa@mail.ru

Tatyana Somova
Navigation, Guidance and Control
Samara State Technical University
Samara, Russia
te_somova@mail.ru

Alexey Dobrosotskikh
Electric Power Stations
Samara State Technical University
Samara, Russia
dob_as@mail.ru

Article history:
Received 26.09.2025, Accepted 21.11.2025

Abstract

Nonlinear control problems of a space robot during mooring and docking with a geostationary communications satellite as well as when its on-orbit maintenance – replacement of fuel tanks and other important elements of a satellite's motion control system are considered. These problems are associated with significant changes in the inertial parameters in the satellite-robot mechanical system. Despite this complicating circumstance, the paper shows that the developed control laws are quite effective, which is confirmed by computer simulation.

1 Introduction

Modern geostationary communications satellites (GCS) have a guaranteed lifetime of up to 17 years. To extend the service life of advanced GCS, they are serviced by a space robot-manipulator (SRM), which is docked with the GCS and provides stabilization of the coupled structure in the orbital reference frame (ORF). The following drives are applied in the SRM attitude and orbit control system (AOCS): a gyro moment cluster (GMC) with four gyrodines (GDs) and electric propulsion units (EPUs) based on both plasma and catalytic electric jet engines (EJEs).

The first attempts to create low-orbit satellite communication systems failed in the early 2000s. Currently, this idea is being persistently due to the increased challenges on globality, speed and volume of information exchange. A decent response of the space communications technology [Testoyedov et al., 2017] based on the space geostationary platforms, eliminates these problems for many standard and newest advanced types of communication. Such platforms are assembled in geostationary orbit (GSO) by SRMs using replaceable components and then regularly serviced by the SRM for several decades. Modern research and developments on these topical

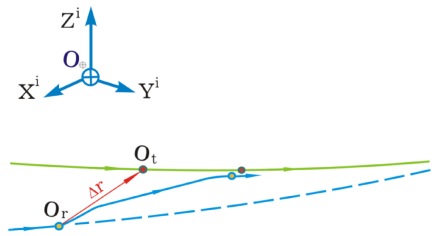

Figure 1. Scheme of the SRM approaching GCS

problems are presented in review articles [Moosavian and Papadopoulos, 2007; Flores-Abad et al., 2014; Li et al., 2019; Ellery, 2019; Papadopoulos et al., 2021]. Nonlinear problems of launching a robot into GSO and its rendezvous with the GCS, the authors studied previously [Somov et al., 2021a; Somov et al., 2021b; Somov et al., 2022c; Somov et al., 2022a]. In the inertial reference frame (IRF) $O_{\oplus}X^iY^iZ^i$ trajectories of target O_t and space robot O_r centers are represented in Fig. 1. We study two problems for robot AOCS: (i) its control at mooring, docking and connection to the GCS using a docking mechanism (DM); (ii) a control when on-orbit servicing the GCS with significant changes in the configuration of docked space vehicles (SVs). This article is an extended version of the paper [Somov et al., 2024] and is related to ones [Aleksandrov and Tikhonov, 2018; Aminov et al., 2019; Somov et al., 2022f].

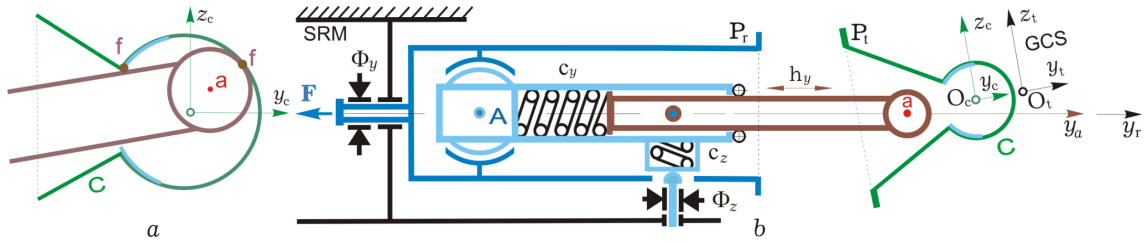

Figure 2. Docking scheme (a) using a "rod-cone" docking mechanism (b)

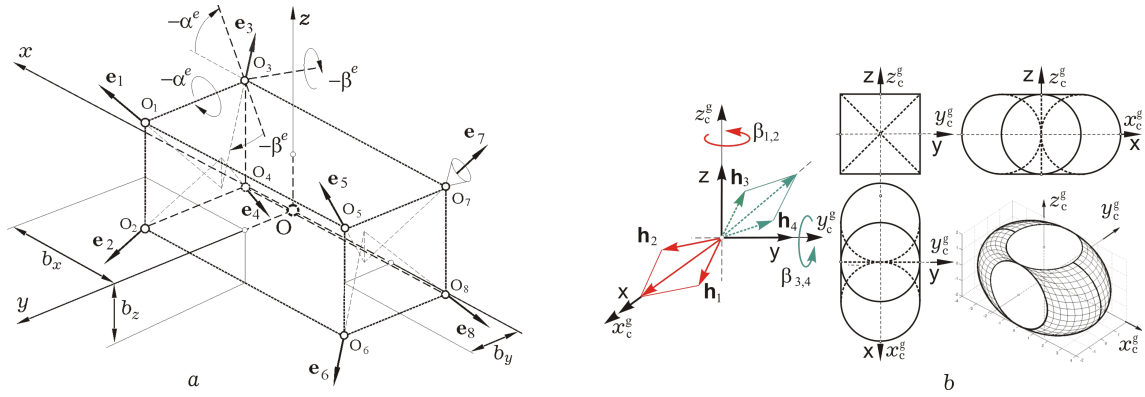

Figure 3. The schemes of EPU with catalytic EJEs (a) and GMC based on 4 gyrodines (b)

2 Considered nonlinear problems

The fundamentals of the theory and technology of spacecraft docking are presented in the well-known monograph [Syromyatnikov, 1984]. In the applied docking mechanism, an active assembly containing a rod and a passive assembly in the form of a receiving cone are distinguished, see Fig. 2 and also some details in our article [Somov et al., 2022d]. At one end of the rod (brown) there is a spherical head of increased diameter with a center at point a (red), Fig. 2a. The rod with a spherical head is a part of the DM active assembly, Fig. 2b. Here, the other end of the rod is elastically fixed in the inner cage (blue color) of the active assembly, which allows both linear movement of the rod along the longitudinal axis y_a, and its angular movement around the transverse axes x_a and z_a with respect to point A, see Fig. 2b. Moreover, the outer cage (dark blue) of the active assembly with a flat docking ring $\mathrm{P_r}$ can move along the longitudinal axis y_r of the SRM, see Fig. 2b. A passive assembly in the form of a receiving cone C (green) with a socket and a flat docking ring $\mathrm{P_t}$ is rigidly fixed on the GCS body, see Fig. 2b.

The SRM docking with the GCS contains three sequentially performed stages, namely 1) a mooring, 2) a contraction, and 3) an alignment and fixation, which are briefly described below.

1) When mooring the SRM to the GCS, the rod head, after several collisions with the surface of the receiving cone C, penetrates into the nest through its neck with an electromechanical shutter, which is marked in blue in Fig. 2. When this event occurs, the shutter operates and reduces the passage diameter of the socket neck to the diameter of the rod cross section. As a result, between the rod and the inner surface of the nest, together with the shutter, a primary mechanical connection arises, in the general case at two points f, see Fig. 2a. Further, the absorption of the kinetic energy of the spatial relative motion of two spacecraft in the docking mechanism occurs due to its elastically damping mechanical bonds with forward deformations h_i, $i = x, y, z$, of springs with stiffness coefficients c_i and generalized forces of both viscous and dry friction realized by the frictions Φ_i, see notation in Fig. 2b. After the velocities of all DM coordinates decay to an acceptable level, the mooring is completed and a coupling of assemblies is formed with small changes in their forward and angular mismatches.

2) The contraction of assemblies along the SRM longitudinal axis y_r is implemented by a drive of the "screw-nut" class with a force vector $\mathbf{F}$ for the outer cage of the active assembly, see Fig. 2b.

3) The alignment of the docking rings $\mathrm{P_r}$ of an active and $\mathrm{P_t}$ of a passive assembly and next fixing of their mutual position is carried out by electromechanical drives of the docking mechanism.

In these two AOCS modes, the main drives are the EPU with 8 catalytic EJEs (Fig. 3a) which use pulse-width modulation (PWM) of their thrust and the GMC with 4 GDs by the well-known *2-SPE* scheme [Somov et al., 2022a; Somov et al., 2022g], Fig. 3b.

Figure 4 shows a simplified scheme of the resulting rigid coupling of the SRM and GCS after their docking is completed. The solar array panels of the SRM and GCS are not presented here, the onboard manipulator of an anthropomorphic structure (Fig. 5) with 4 physical links ($l_{01} = l_{03} \equiv 0$) and 6 degrees of freedom which correspond to the angular coordinates q_s, $s = 1 \div 6$ is in the stowed state and the dimensions of structural elements, including EPU fuel tanks, are indicated in meters.

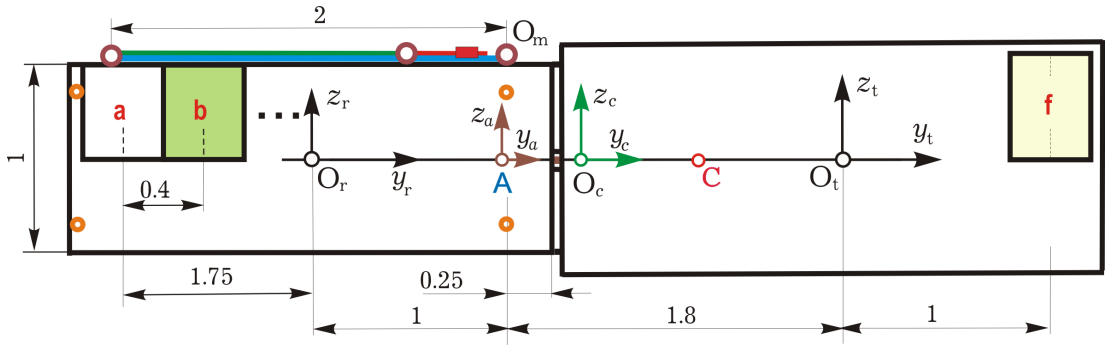

Figure 4. Docking result: a diagram of a rigid mechanical coupling between a space robot and a geostationary satellite

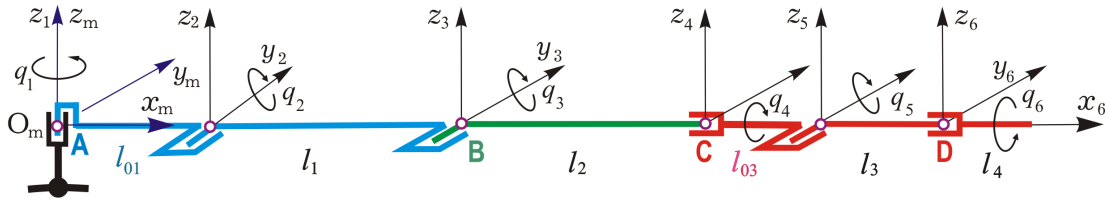

Figure 5. Kinematic diagram of the onboard manipulator of the space robot

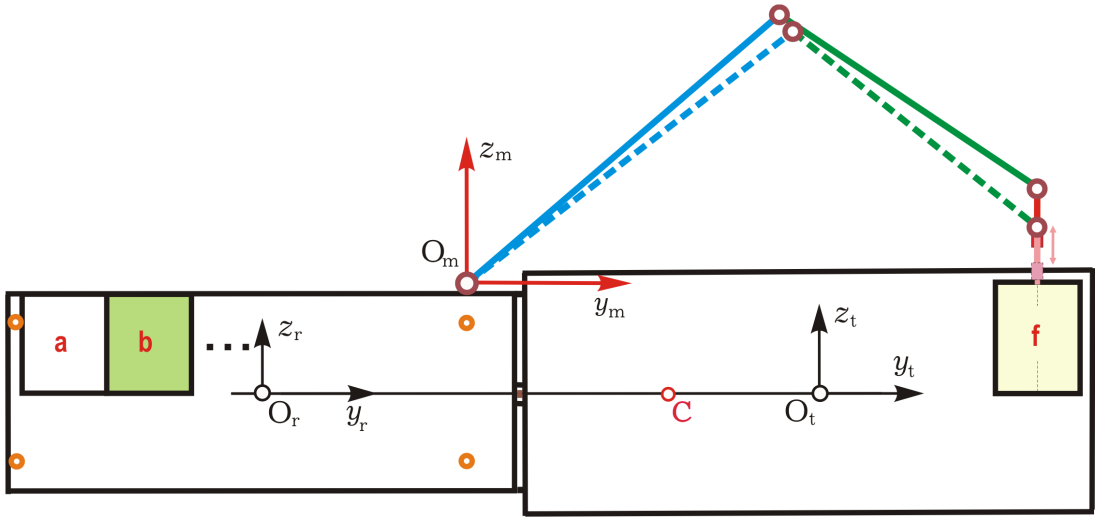

Figure 6. The control scheme of the manipulator when changing fuel tanks of the communications satellite EPU

The nonlinear problem of SRM control when changing the fuel tanks of the GCS propulsion unit was considered in [Butyrin et al., 2022; Somov et al., 2022b; Somov et al., 2022e]. Here, it was assumed that the SRM and GCS are rigidly docked, and mechanical manipulations with the fuel tanks occur automatically, see Fig. 6. The end link of the manipulator contains a special mechanism – a key, which rigidly holds the fuel tank when the key is closed. The strategy of changing the EPU fuel tanks uses the following provisions: (i) empty tanks are moved by the manipulator from the GCS containers to the SRM containers, and the fuel-filled tanks – from the SRM containers to the GCS containers; (ii) the installation of tanks in containers is completed by their automatic mechanical fixation; (iii) switching on / off of the fuel supply system from a tank to the EPU is carried out by a mechatronic module built into each GCS container.

3 Mathematical models and discussion of problems

To describe motions of the SRM and GSS in the modes under study, along with the equatorial IRF $\mathbf{I}_\oplus$ we use the coupled reference frame $Oxyz$ with origin at the pole O, which coincides with the SRM body reference frame (BRF) $\mathbf{B}$ $\mathrm{O_r}x_\mathrm{r}y_\mathrm{r}z_\mathrm{r}$ (robot); orbital reference frame (ORF) $\mathbf{O}$ $(Ox^\mathrm{o}y^\mathrm{o}z^\mathrm{o})$ with standard unit vectors of radial $\mathbf{r}^\mathrm{o}$, transversal $\boldsymbol{\tau}^\mathrm{o}$ and binormal $\mathbf{n}^\mathrm{o}$; the reference frame $\mathrm{O_t}x_\mathrm{t}y_\mathrm{t}z_\mathrm{t}$ associated with GCS (target) at its mass center $\mathrm{O_t}$; the reference frame $\mathrm{A}x_ay_az_a$ associated with the rod of the active assembly and the reference frame $\mathrm{O_c}x_\mathrm{c}y_\mathrm{c}z_\mathrm{c}$ of the receiving cone C of the passive assembly, see Figs. 2 and 4.

The manipulator is fixed to the SRM body by a rack (master) at a point $\mathrm{O_m}$ of the manipulator reference frame $\mathrm{O_m}x_\mathrm{m}y_\mathrm{m}z_\mathrm{m}$, which is fixed in the robot's body reference frame $\mathrm{O_r}x_\mathrm{r}y_\mathrm{r}z_\mathrm{r}$, see Fig. 6.

We use the notation $\{\cdot\} = \mathrm{col}(\cdot)$, $[\cdot] = \mathrm{line}(\cdot)$, $\langle\cdot,\cdot\rangle$, $[\cdot\times]$, $(\cdot)^{\mathrm{t}}$, $[\mathbf{a}\times]$ and $\circ$, $\tilde{}$ for vectors , matrices and quaternions, as well as matrix $[\alpha]_i$ of a standard elementary rotation about the i-th axis by the angle α for $i = 1,2,3 \equiv 1 \div 3$. Orientation of the BRF $\mathbf{B}$ in the IRF $\mathbf{I}_\oplus$ is defined by the quaternion $\mathbf{\Lambda} = (\lambda_0, \boldsymbol{\lambda})$, where $\boldsymbol{\lambda} = \{\lambda_i\}$, vector of modified Rodrigues parameters (MRP) $\boldsymbol{\sigma} = \{\sigma_i\} = \mathbf{e}\ \tan(\Phi/4)$ with unit vector $\mathbf{e}$ of the Euler axis and angle Φ of its own rotation.

In the IRF $\mathbf{I}_\oplus$ kinematic equations for vector $\mathbf{r}_{\mathrm{r}}$ of the SRM location, the quaternion $\mathbf{\Lambda}$ and the MRP vector $\boldsymbol{\sigma}$ have the form $\dot{\mathbf{r}}_{\mathrm{r}} = \mathbf{r}'_{\mathrm{r}} + \boldsymbol{\omega}\times\mathbf{r}_{\mathrm{r}} \equiv \mathbf{v}_r$; $\dot{\mathbf{\Lambda}} = \mathbf{\Lambda}\circ\boldsymbol{\omega}/2$; $\dot{\boldsymbol{\sigma}} = (1/4)[(1-\sigma^2)\boldsymbol{\omega} + 2\boldsymbol{\sigma}\times\boldsymbol{\omega} + 2\langle\boldsymbol{\sigma},\boldsymbol{\omega}\rangle\boldsymbol{\sigma}]$, where vector $\boldsymbol{\omega}$ represents the SV angular velocity and the notation $(\cdot)'$ is used for the local time derivative. Orientation of the basis $\mathbf{O}$ in basis $\mathbf{I}_\oplus$ is determined by the angles of yaw $\phi_1 = \psi$, roll $\phi_2 = \varphi$ and pitch $\phi_3 = \theta$ in sequence 132, by quaternion $\mathbf{\Lambda}^{\mathrm{o}}$ and a matrix $\mathbf{C}^{\mathrm{o}} = [\phi_2]_2\,[\phi_3]_3\,[\phi_1]_1$ for a coordinate transition from ORF to BRF. The orientation error of basis $\mathbf{B}$ into basis $\mathbf{O}$ is determined by quaternion $\mathbf{E} = \tilde{\mathbf{\Lambda}}^{\mathrm{o}}\circ\mathbf{\Lambda} \equiv (e_0, \mathbf{e})$, a matrix $\mathbf{C}^{\mathrm{e}} = \mathbf{I}_3 - 2[\mathbf{e}\times]\mathbf{Q}^{\mathrm{t}}_{\mathrm{e}}$ with $\mathbf{Q}_{\mathrm{e}} = \mathbf{I}_3 e_0 + [\mathbf{e}\times]$, as well as by error vector $\delta\boldsymbol{\phi} \equiv \{\delta\phi_i\} = \{2e_0 e_i\}$ and the MRP vector $\boldsymbol{\sigma}^{\mathrm{e}} = \{\sigma^{\mathrm{e}}_i\} = \mathbf{e}^{\mathrm{e}}\ \tan(\Phi^{\mathrm{e}}/4)$. Moreover, the angular velocity error vector is calculated as $\delta\boldsymbol{\omega} = \boldsymbol{\omega} - \mathbf{C}^{\mathrm{e}}\boldsymbol{\omega}^{\mathrm{o}}(t)$, where vector $\boldsymbol{\omega}^{\mathrm{o}}(t)$ represents the rotation velocity of basis $\mathbf{O}$ in the basis $\mathbf{I}_\oplus$. In the EPU scheme with 8 catalytic EJEs (Fig. 3*a*) we present the unit vectors $\mathbf{e}_p$, $p = 1 \div 8$ of EJE's nozzle axes. We assume that vector $\boldsymbol{\rho}_p \in \{\pm b_x, \pm b_y, \pm b_z\}\ \forall p$ with a module $|\boldsymbol{\rho}_p| = \rho$ defines the point O_p at which the thrust vector of p-th EJE is applied.

Each catalytic EJE has the PWM of its thrust $p_p(t)$, described by the nonlinear continuous-discrete relation $p_p(t) = \mathrm{P^m}\,\mathrm{PWM}(t - T^{\mathrm{e}}_{zu}, t_r, \tau_m, \mathrm{v}_{pr})\ \forall t \in [t_r, t_{r+1})$, $t_{r+1} = t_r + T^{\mathrm{e}}_u$, $r \in \mathbb{N}_0 \equiv [0,1,2,\dots)$ with a period T^{e}_u and a time delay T^{e}_{zu}. Here, $\mathrm{P^m}$ is the nominal value of a thrust, similar for all catalytic EJEs, and the function

$$\mathrm{PWM}(t, t_r, \tau_m, \mathrm{v}_{pr}) \equiv \begin{cases} \mathrm{sign}\,\mathrm{v}_{pr} & t \in [t_r, t_r + \tau_{pr}), \\ 0 & t \in [t_r + \tau_{pr}, t_{r+1}); \end{cases}$$

$$\tau_{pr} \equiv \begin{cases} 0 & |\mathrm{v}_{pr}| \le \tau_m, \\ \mathrm{sat}\,(T^{\mathrm{e}}_u,\ |\mathrm{v}_{pr}|) & |\mathrm{v}_{pr}| > \tau_m. \end{cases}$$

In the BRF, a thrust vector of p-th EJE is formed as $\mathbf{p}_p(t) \equiv \{\mathrm{p}_p\} = -p_p(t)\,\mathbf{e}_p$, and vectors of the EPU thrust $\mathbf{P}^{\mathrm{e}}$ and torque $\mathbf{M}^{\mathrm{e}}$ are computed by the formulas $\mathbf{P}^{\mathrm{e}} = \Sigma\,\mathbf{p}_p(t)$ and $\mathbf{M}^{\mathrm{e}} = \Sigma\,[\boldsymbol{\rho}_p\times]\mathbf{p}_p(t)$.

A collinear GD pair is named as *Scissored Pair Ensemble* (*SPE*) [Crenshaw, 1973]. Column $\boldsymbol{\mathcal{H}}(\boldsymbol{\beta}) \equiv \mathrm{h}_g\mathbf{h}(\boldsymbol{\beta}) = \mathrm{h}_g\Sigma\mathbf{h}_p(\beta_p)$ with the columns $\boldsymbol{\beta} \equiv \{\beta_p\}$, $p = 1 \div 4$ and $\mathbf{h}(\boldsymbol{\beta}) \in \boldsymbol{\mathcal{S}} \subset \mathbb{R}^3$, presents the angular momentum (AM) vector of the GMC by scheme *2-SPE* (Fig. 3*b*) [Somov et al., 2021b], where h_g is the own AM of each GD. With $|\mathbf{h}_p| = 1$, in the park state this scheme has normed AM vector $\mathbf{h}(\boldsymbol{\beta}) = \mathbf{0}$. In canonical reference frame $\mathrm{O}x^{\mathrm{g}}_{\mathrm{c}}y^{\mathrm{g}}_{\mathrm{c}}z^{\mathrm{g}}_{\mathrm{c}}$ (Fig. 3*b*), we will count the angles β_1, β_2 from the $x^{\mathrm{g}}_{\mathrm{c}}$ axis, and angles β_3, β_4 – from the $z^{\mathrm{g}}_{\mathrm{c}}$ axis. Using the notation $S_p \equiv \sin\beta_p$ and $C_p \equiv \cos\beta_p$, the GD's AM unit vectors $\mathbf{h}_p$ have following projections:

$$x_1 = C_1; x_2 = C_2; x_3 = S_3;\quad x_4 = S_4;$$
$$y_1 = S_1; y_2 = S_2; z_3 = C_3; z_4 = C_4.$$

Then using the normed AM vector $\mathbf{h}(\boldsymbol{\beta}) = \{x, y, z\} = \{\Sigma x_p, \Sigma y_p, \Sigma z_p\}$ and matrix $\mathbf{A}_{\mathrm{h}}(\boldsymbol{\beta}) = \partial\mathbf{h}(\boldsymbol{\beta})/\partial\boldsymbol{\beta}$ we obtain the control torque vector of the GMC $\mathbf{M}^{\mathrm{g}} = \{\mathrm{M}^{\mathrm{g}}_i\}$ presented by the nonlinear digital-continuous relations

$$\mathbf{M}^{\mathrm{g}} = -\boldsymbol{\mathcal{H}}' = -\mathrm{h}_g\mathbf{A}_{\mathrm{h}}(\boldsymbol{\beta})\,\mathbf{u}^{\mathrm{g}}_k(t);\ \dot{\boldsymbol{\beta}} = \mathbf{u}^{\mathrm{g}}_k(t) \equiv \{\mathrm{u}^{\mathrm{g}}_{pk}(t)\}$$

with controls $\mathrm{u}^{\mathrm{g}}_{pk}(t) = \mathrm{Zh}[\mathrm{sat}(\mathrm{qntr}(u^g_{pk}, u^{\mathrm{o}}_g), u^{\mathrm{m}}_g), T_u]$; $\mathrm{qntr}(x,a) \equiv aE((x/a + (\mathrm{sign}\,x)/2)$ at integer symbol $E(\cdot)$, $\mathrm{Zh}(x_k, T_u) \equiv x_k\,\forall t \in [t_k, t_{k+1})$, $k \in \mathbb{N}_0$ and a period T_u. When we consider the SRM as a rigid body with a mass m_{r} and an inertia tensor $\mathbf{J}_{\mathrm{r}}$, then its spatial dynamics is represented in the IRF as follows

$$\begin{aligned} &\mathbf{r}' + \boldsymbol{\omega}\times\mathbf{r} = \mathbf{v};\ m(\mathbf{v}' + \boldsymbol{\omega}\times\mathbf{v}) = \mathbf{P}^{\mathrm{e}} + \mathbf{F}^{\mathrm{d}}; \\ &\dot{\mathbf{\Lambda}} = \mathbf{\Lambda}\circ\boldsymbol{\omega}/2;\ \mathbf{J}_{\mathrm{r}}\dot{\boldsymbol{\omega}} + \boldsymbol{\omega}\times\mathbf{G} = \mathbf{M}^{\mathrm{g}} + \mathbf{M}^{\mathrm{e}} + \mathbf{M}^{\mathrm{d}}, \end{aligned} \tag{1}$$

where vector $\mathbf{G} = \mathbf{J}_{\mathrm{r}}\boldsymbol{\omega} + \boldsymbol{\mathcal{H}}$, and vectors $\mathbf{F}^{\mathrm{d}}$ and $\mathbf{M}^{\mathrm{d}}$ represent external disturbing forces and torques.

For the SRM attitude guidance law $\mathbf{\Lambda}^p$, $\boldsymbol{\omega}^p$, $\boldsymbol{\varepsilon}^p$ in the IRF, the attitude error quaternion $\mathbf{E} = (e_0, \mathbf{e}) = \tilde{\mathbf{\Lambda}}^p\circ\mathbf{\Lambda}$ with $\mathbf{e} = \{e_i\}$ corresponds to the attitude error matrix $\mathbf{C}^{\mathrm{e}} = \mathbf{I}_3 - 2[\mathbf{e}\times]\mathbf{Q}^{\mathrm{t}}_{\mathrm{e}}$ with $\mathbf{Q}_{\mathrm{e}} = \mathbf{I}_3 e_0 + [\mathbf{e}\times]$ and MRP vector $\boldsymbol{\sigma}^{\mathrm{e}} = \mathbf{e}^{\mathrm{e}}\ \tan(\Phi^{\mathrm{e}}/4)$ as well as angular error vector $\delta\boldsymbol{\phi} = \{\delta\phi_i\} = 4\boldsymbol{\sigma}^{\mathrm{e}}$, and the angular velocity error vector $\delta\boldsymbol{\omega} = \boldsymbol{\omega} - \mathbf{C}^{\mathrm{e}}\boldsymbol{\omega}^p$. For the SRM attitude control, a vector $\delta\boldsymbol{\phi}$ is discrete filtered and mismatch vector $\boldsymbol{\epsilon}^{\mathrm{f}}_k = -\boldsymbol{\phi}^{\mathrm{f}}_k$ as well vectors $\boldsymbol{\omega}_k$ and $\mathbf{G}_k = \mathbf{J}\boldsymbol{\omega}_k + \boldsymbol{\mathcal{H}}_k$ are determined to calculate the GMC control torque vector $\mathbf{M}^{\mathrm{g}}_k$ as follows

$$\begin{aligned} &\mathbf{g}^{\mathrm{g}}_{k+1} = k^{\mathrm{g}}_b\mathbf{g}^{\mathrm{g}}_k + k^{\mathrm{g}}_c\boldsymbol{\epsilon}^{\mathrm{f}}_k;\ \tilde{\mathbf{m}}_k = k^{\mathrm{g}}_u(\mathbf{g}^{\mathrm{g}}_k + k^{\mathrm{g}}_p\boldsymbol{\epsilon}^{\mathrm{f}}_k); \\ &\mathbf{M}^{\mathrm{g}}_k = \boldsymbol{\omega}_k\times\mathbf{G}_k + \mathbf{J}(\mathbf{C}^{\mathrm{e}}_k\boldsymbol{\varepsilon}^p_k + [\mathbf{C}^{\mathrm{e}}_k\boldsymbol{\omega}^p_k\times]\boldsymbol{\omega}_k + \tilde{\mathbf{m}}_k), \end{aligned} \tag{2}$$

which is distributed between four GDs by analytical relations [Matrosov and Somov, 2004; Somov et al., 2022a]. As a result, the GMC digital control vector $\mathbf{u}^{\mathrm{g}}_k(t) = \mathbf{u}^{\mathrm{g}}_k$ is formed $\forall\, t \in [t_k, t_{k+1})$.

When dynamical research of mooring & docking for the SRM with GCS, we studied variations in the differences in the velocity vectors of their both forward $\Delta\mathbf{v} = \{\Delta\mathrm{v}_i\}$ and angular $\Delta\boldsymbol{\omega} = \{\Delta\omega_i\}$ movements, as well as changes in the vector $\Delta\boldsymbol{\phi} = \{\Delta\phi_i\}$ mutual angular error. A vector form of Euler-Lagrange equations [Lur'e, 1961] is used to research of mated SRM & GCS with vector $\mathbf{L} = \mathrm{m}\boldsymbol{\rho}_{\mathrm{c}}$ of static mechanical moment:

$$\begin{aligned} \mathrm{m}\dot{\mathbf{v}}_{\mathrm{o}} + [\mathbf{L}\times]^{\mathrm{t}}\dot{\boldsymbol{\omega}} &= \boldsymbol{\omega}\times(\mathbf{L}\times\boldsymbol{\omega}) \\ &\quad -\Sigma_i\mathrm{m}_i(2\boldsymbol{\omega}\times\boldsymbol{\rho}'_i + \boldsymbol{\rho}''_i) + \mathbf{P}^{\mathrm{e}} + \mathbf{F}^{\mathrm{d}}; \\ [\mathbf{L}\times]\dot{\mathbf{v}}_{\mathrm{o}} + \mathbf{J}\,\dot{\boldsymbol{\omega}} &= -\boldsymbol{\omega}\times\mathbf{G} - \mathbf{R} + \mathbf{M}^{\mathrm{g}} + \mathbf{M}^{\mathrm{e}} + \mathbf{M}^{\mathrm{d}} \end{aligned}$$

with vectors $\dot{\mathbf{v}}_{\mathrm{o}} = \mathbf{v}'_{\mathrm{o}} + \boldsymbol{\omega}\times\mathbf{v}_{\mathrm{o}}$; $\boldsymbol{\rho}'_i = \Sigma_s((\partial\boldsymbol{\rho}_i/\partial q_s)\,\dot{q}_s)$; $\boldsymbol{\rho}''_i = \Sigma_s((\partial\boldsymbol{\rho}_i/\partial q_s)\,\ddot{q}_s + \Sigma_k(\partial^2\boldsymbol{\rho}_i/\partial q_k\,\partial q_s))$ and

$$\begin{aligned} \mathbf{R} = \Sigma_i(&\mathbf{J}_i\dot{\boldsymbol{\omega}}_i + \boldsymbol{\omega}\times\mathbf{J}_i\boldsymbol{\omega}_i + \boldsymbol{\omega}_i\times\mathbf{J}_i(\boldsymbol{\omega} + \boldsymbol{\omega}_i) \\ &+\mathrm{m}_i\boldsymbol{\rho}_i\times(\boldsymbol{\omega}\times(\boldsymbol{\omega}\times\boldsymbol{\rho}_i) + 2\boldsymbol{\omega}\times\boldsymbol{\rho}'_i + \boldsymbol{\rho}''_i)), \end{aligned}$$

supplemented by standard Lagrange equations for the manipulator degrees of mobility q_s. In their right-hand parts, along with the generalized forces Q_s, representing the torques by electromechanical drives, there are mechanical torques [Lur'e, 1961; Somov et al., 2019], which are caused by the spatial movement of this mate.

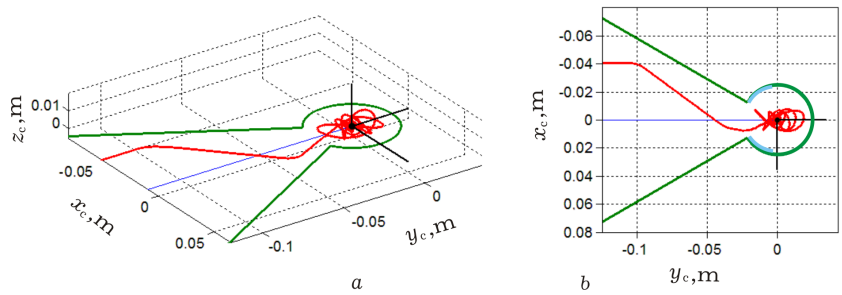

Figure 7. The trajectory of the impact movement of the rod's head center when mooring the SRM to GCS

After docking is complete, distance from the SRM's container **a** to tank in the GCS container **f** is 5.6 m. It follows from simple geometric calculations that the condition $l_1 + l_2 \geq 3.3$ m must be met for the sum of the lengths of the first two links of the manipulator. These conditions are satisfied by a manipulator with a kinematic scheme in Fig. 5 for link lengths $l_1 = 2$ m, $l_2 = 1.5$ m, $l_3 = 0.5$ m, when $l_4 = 0$ without a tank and $l_4 = 0.25$ m with a tank. So, there are following restrictions on angular coordinates: $-\pi \leq q_1 \leq \pi, 0 \leq q_2 \leq \pi$ and $-\pi \leq q_s \leq \pi,\ s = 3 \div 6$.

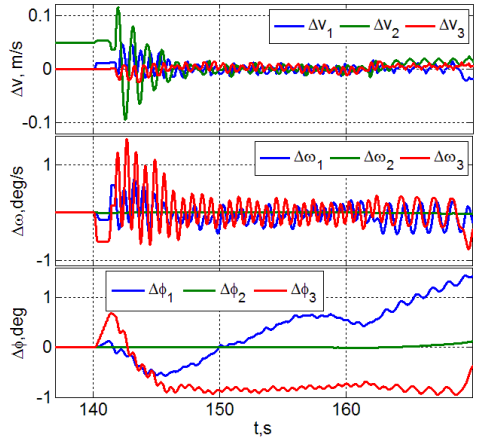

Figure 8. The relative coordinates when the SRM mooring to GCS

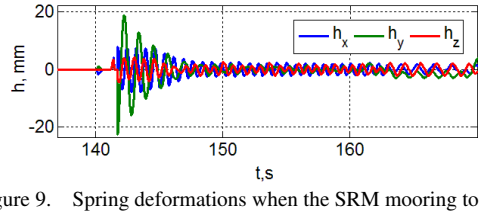

Figure 9. Spring deformations when the SRM mooring to GCS

4 Computer simulation results

To assess the required torques of manipulator's drives, the column $\mathbf{Q} = \{Q_s\}$ composed of torques Q_s on output shafts is calculated, when their load is represented by inertia forces only. In this case, vector $\mathbf{Q}$ is calculated by standard ratio $\mathbf{Q} = \mathbf{A}(\mathbf{q})\ddot{\mathbf{q}} + \mathbf{B}(\mathbf{q}, \dot{\mathbf{q}})\dot{\mathbf{q}}$ when explicit dependencies of matrices $\mathbf{A}$ and $\mathbf{B}$ on column $\mathbf{q} = \{q_s\}$ composed of the angular coordinates q_s.

A computer study of the control systems for SRM and GCS during their mooring was carried out with the parameters presented in [Somov et al., 2022d].

Figure 7 shows the trajectory of the rod's head center (point **a** in red, see Fig. 2) when mooring the SRM to the GCS. Here, the 3D-mapping of the trajectory is shown in Fig.7*a*, and the projection of this trajectory onto the plane $x_c O_c y_c$ of the receiving cone's reference frame – in Fig.7*b*.

The important stage of the SRM mooring $\forall t \in [140, 161.7)$ s with impact movements of the rod head in socket and absorption of kinetic energy is presented in Figs. 8 and 9.

During this research, the possibilities were also studied on increasing a viscous damping of oscillations in the active assembly using rheological suspensions controlled by electromagnetic field.

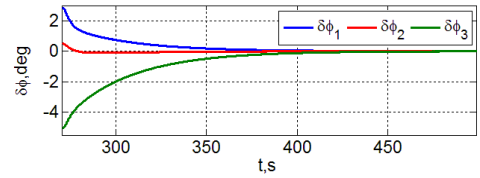

Figure 10. Orientation errors when docking the SRM and GCS

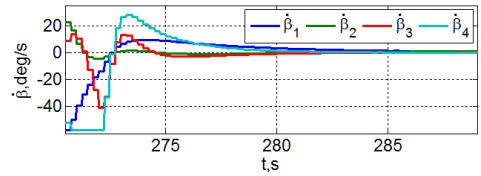

Figure 11. The GMC control commands at docking completion

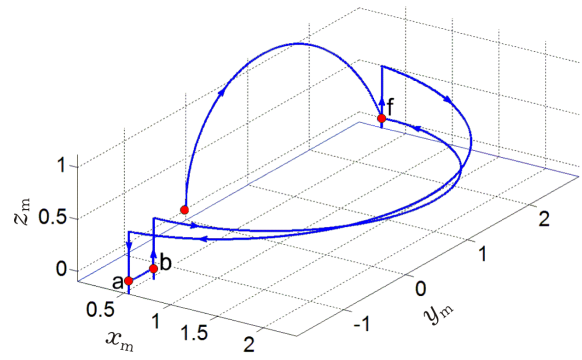

Figure 12. Trajectory of the manipulator grip with a fuel tank

Figure 10 represents the orientation errors of the mate after two SV docking, and Fig. 11 – the GMC digital control commands when the docking is completed.

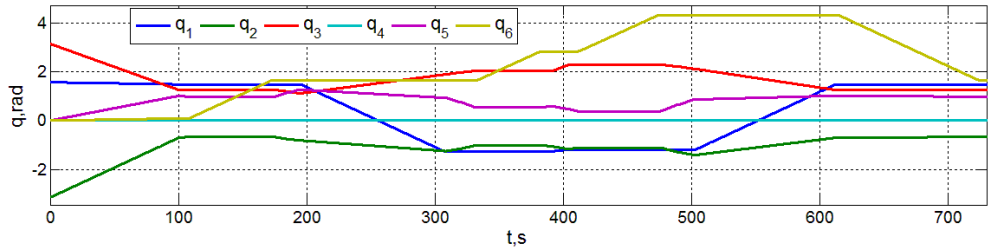

Figure 13. Changing the angular coordinates of the manipulator when replacing the fuel tank

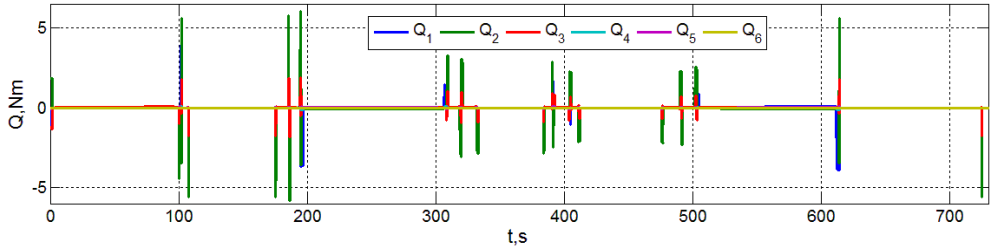

Figure 14. Estimates of the required torques on the output shafts of the manipulator drives

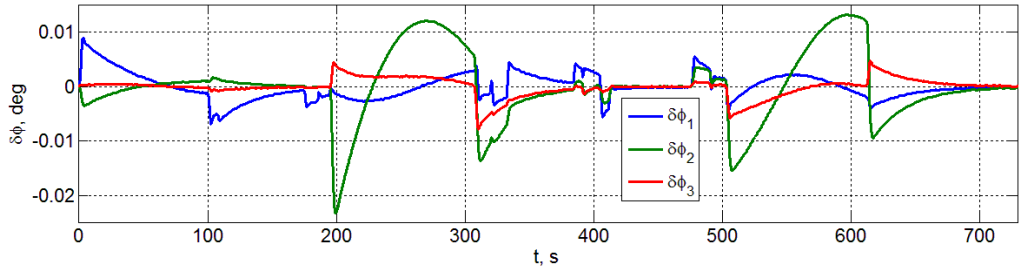

Figure 15. Angular deviations of the BRF relative to the ORF when changing the fuel tank

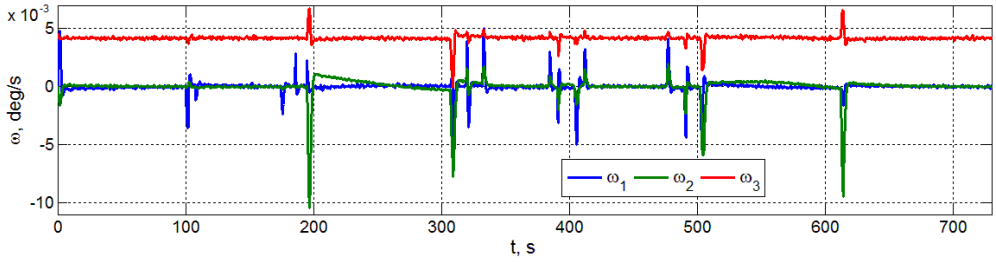

Figure 16. Change in the angular velocities of the SRM and GCS mate when changing the fuel tank

The kinematic model of the manipulator necessarily includes formulas for solving direct and inverse problems [Fu et al., 1987]. The synthesis of manipulator guidance laws during its transitions between target states with given boundary conditions includes two aspects: (i) calculation of the initial $t_{\rm i}$ and final $t_{\rm f}$ time moments as well as duration $T_{\rm m} = t_{\rm f} - t_{\rm i}$ of each stage; (ii) forming the dependencies of angles $q_s(t)$, velocities $\dot{q}_s(t)$ and accelerations $\ddot{q}_s(t)$ with restrictions on angles as well as modules of velocities and accelerations, namely $|\dot{q}_s(t)| \le \dot{q}^*, |\ddot{q}_s(t)| \le \ddot{q}^*\ \forall t \in T_{\rm m} \equiv [t_{\rm i}, t_{\rm f}]$ at the specified values of parameters $\dot{q}^*$ and $\ddot{q}^*$. Adaptive-robust algorithms with a reference guidance model were applied for digital control of electric drives according to the manipulator degrees of mobility [Krut'ko, 1991].

When changing fuel tanks, the manipulator performs the typical actions: 1) the grab is transferred from initial position first to the GCS container with an empty tank **f** (Figs. 6 and 12), which is then moved to an empty container **a** of the SRM; 2) the grab goes to the SRM container **b** and then moves the full fuel tank **b** to the GCS container **f**. Changes in the links coordinates and estimates of required drives torques when replacing a fuel tank weighing 90 kg are presented in Figs. 13 and 14.

When using gearboxes with a gear ratio of 1:400, the required torques will not exceed 10 Nm, which allows the use of motors with a rated torque of 0.025 Nm and a maximum angular velocity of 100 rpm. Changes in the orientation parameters of the mate in the ORF when changing the tank, are represented in Figs. 15 and 16.

Methods have been developed for robust control of a space robot during the in-flight maintenance of a GCS by replacement of its AOCS components. Detailed results are represented in [Somov et al., 2022e].

5 Conclusions

Methods have been developed to control a space robot-manipulator during its mooring, docking and subsequent rigid connection to a geostationary communications satellite using a docking mechanism of the "rod-cone" class. The developed methods and digital algorithms for robust control of a space robot are briefly presented. Such maintenance leads to significant changes in the inertial parameters of the rigid connection between the space robot and geostationary satellite, and also to nonlinear control problems.

The article indicates a simple and reliable way to control a space robot in the studied modes. The results of computer simulation are presented, confirming the effectiveness of the created methods.

References

Aleksandrov, A. and Tikhonov, A. (2018). Rigid body stabilization under time-varying perturbations with zero mean values. *Cybernetics and Physics*, **7** (1), pp. 5–10.

Aminov, R., Shmyrov, A., and Shmyrov, V. (2019). Impulse control flight to the invariant manifold near collinear libration point.*Cybernetics and Physics*, **8** (2), pp. 51–57.

Butyrin, S., Somov, Y., Somov, S., and Somova, T. (2022). Control of the robot-manipulator when changing fuel tanks of the geostationary satellite propulsion unit. *Izvestia RAS SamSC*, **24** (1), pp. 96–104.

Crenshaw, J. (1973). 2-SPEED, a single-gimbal moment gyro attitude control system. *AIAA Paper*, (73-895), pp. 1–10. doi:10.2514/6.1973-895.

Ellery, A. (2019). Tutorial review on space manipulators for space debris mitigation. *Robotics*, **8** (2), pp. 1–52.

Flores-Abad, A., Ma, O., et al. (2014). A review of space robotics technologies for on-orbit servicing. *Prog. Aerosp. Sci.*, **68** (5), pp. 1–26.

Fu, K., Gonzalez, R., and Lee, C. (1987). *Robotics: Control, Sensing, Vision, and Intelligence*. McGraw-Hill, New York.

Krut'ko, P. (1991). *Control of Robots Executive Systems*. Nauka, Moscow.

Li, W., Cheng, D., Liu, X., et al. (2019). On-orbit service (OOS) of spacecraft: A review of engineering developments. *Prog. Aerosp. Sci.*, **108** (2), pp. 32–120.

Lur'e, A. (1961). *Analytical Mechanics*. Fizmatgiz, Moscow.

Matrosov, V. and Somov, Y. (2004). Nonlinear problems of spacecraft fault tolerant control systems. In Sivasundaram, S., editor, *Nonlinear Problems in Aviation and Aerospace. Vol. 12: Advanced in Dynamics and Control*, pp. 309–331. CRC Press / Taylor & Francis.

Moosavian, S. and Papadopoulos, E. (2007). Free-flying robots in space: an overview of dynamics modeling, planning and control. *Robotica*, **25** (5), pp. 537–547.

Papadopoulos, E., Aghili, F., Ma, O., and Lampariello, R. (2021). Robotic manipulation and capture in space: A survey. *Front. Robot. AI*, **8** (686723), pp. 1–36.

Somov, Y., Butyrin, S., and Somov, S. (2021a). Additional launching and approach of space robot for servicing a geostationary satellite. *Izvestia RAS SamSC*, **23** (2), pp. 75–83.

Somov, Y., Butyrin, S., and Somov, S. (2021b). Autonomous attitude and orbit control of a space robot inspecting a geostationary satellite. *J. Phys. Conf. Ser.*, **1864** (012132), pp. 1–7.

Somov, Y., Butyrin, S., and Somov, S. (2022a). Attitude and orbit control of a space robot at additional launching and approaching a geostationary satellite. *Current Chinese Science*, **2** (3), pp. 173–182.

Somov, Y., Butyrin, S., and Somov, S. (2022b). Control of a space robot-manipulator at replacing the fuel tanks of a geostationary satellite. In *Proc. 2022 16th Int. Conf. on Stability and Oscillations of Nonlinear Control Systems*, Moscow, pp. 1–4.

Somov, Y., Butyrin, S., Somov, S., and Somova, T. (2019). Control of robot-manipulator during its preparation and capture of a passive satellite. *MESA*, **10** (3), pp. 421–432.

Somov, Y., Butyrin, S., Somov, S., and Somova, T. (2022c). Attitude and orbit control of a space robot at launching, rendezvous and checking the geostationary satellite state. *MESA*, **13** (1), pp. 11–24.

Somov, Y., Butyrin, S., Somov, S., and Somova, T. (2022d). Dynamics of mooring and docking of a space robot-manipulator with a geostationary satellite. *Izvestia RAS SamSC*, **24** (4), pp. 155–160.

Somov, Y., Butyrin, S., Somov, S., and Somova, T. (2022e). Robust control of a space robot-manipulator when servicing a geostationary communications satellite. *Izvestia RAS SamSC*, **24** (4), pp. 161–167.

Somov, Y., Butyrin, S., and Somova, T. (2022f). A space robot control at approaching and inspecting a geostationary satellite state. *Cybernetics and Physics*, **11** (1), pp. 30–36.

Somov, Y., Butyrin, S., Somova, T., and Somov, S. (2022g). Space robot motion control during rendezvous and visual inspecting a geostationary satellite state. *IFAC-PapersOnLine*, **55** (22), pp. 61–66.

Somov, Y., Somov, S., Butyrin, S., and Somova, T. (2024). Nonlinear problems of guidance and control of a space robot-manipulator in geostationary orbit. *MESA*, **15** (4), pp. 1–11.

Syromyatnikov, V. S. (1984). *Docking devices of spacecraft*. Mashinostroyenie, Moscow.

Testoyedov, N., Rayevsky, V., Somov, Y., Titov, G., and Yakimov, Y. (2017). Attitude and orbit control systems of Russian communication, navigation and geodesic satellites: History, present and future. *IFAC-PapersOnLine*, **50** (1), pp. 6422–6427.